

## **Chapter 4 : Unbiased Subsample Displacement Interpolation**

Accurate subsample displacement estimation is a necessity in ultrasound elastography because of the small deformations that occur and the subsequent application of a derivative operation on local displacements. Many of the commonly used subsample estimation techniques introduce significant bias errors. In this chapter an unbiased approach to subsample displacement estimations that consists of two-dimensional windowed-sinc interpolation with numerical optimization is examined. It is shown that a Welch or Lanczos window with Nelder-Mead simplex or regular-step gradient descent optimization is well suited for this purpose. First, a literature review of past efforts for subsample time delay estimation and ultrasound displacement estimation is given. Next, implementation of the new algorithm is described. Finally, the method is compared to the common parabolic and cosine interpolation methods, tradeoffs between precision and computational time are quantified, and optimal parameters are determined. The usefulness of this approach is also proven to not rely on special properties of the image or similarity function by demonstrating its effectiveness after applying the regularization algorithm discussed in Chapter 3.

### **4.1 Previously explored methods for subsample tracking**

Accurate and precise sub-sample estimation of local displacements is critical for ultrasound elastography based applications. The recent movement towards transducers with higher center

frequencies and broader bandwidths with the sampling frequencies barely satisfying the Shannon-Nyquist criterion have also demonstrated the need for accurate sub-sample estimation. Furthermore, noise is introduced into the post-deformation signal. These conditions are a concern when trying to perform ultrasound strain imaging where displacement estimates need precision on the order of micrometers; sample spacing in the axial direction is only  $19\text{ }\mu\text{m}$  for a 40 MHz sampling rate. Cespedes et al. [1] examined the theoretical limit for time delay estimation using cross correlation with parameters from a typical ultrasound system. He found that the standard deviation due to time quantization was 5.7 ns, which is much larger than the Cramer-Rao Lower Bound (CRLB) for the continuous case, 0.024 ns.

#### **4.1.1 Methods that use properties of cross-correlation**

This subsample delay estimation problem has been studied extensively in one-dimension (1D) for the sonar and radar fields, where use of cross-correlation as a similarity metric is dominant. If the signal is approximately narrowband, quadrature subsample delay techniques can be used [2]. Maskell and Woods describe a technique where the shift between signals is not determined by comparing them directly but by comparisons with shifted versions of a reference signal [3]. The total delay is then determined to be the difference between the two delays to the reference signal.

A number of techniques use the fact that phase of the analytic signal's cross-correlation in the vicinity of the signal shift will have a slope equivalent to the nominal centroid frequency and zero crossing at the shift [4, 5]. Marple discusses the theory behind this method, and the scaling that must occur at the DC and Nyquist frequencies when dealing with discrete signals. Grennberg and Sandell described a fast subsample delay estimator calculated with the cross correlation of the delayed signal with the Hilbert transform of the original signal using an arcsine

[6]. Other authors use similar approaches by taking the cross-correlation of base-band analytic signals from both the original and shifted signals [5, 7]. The root is then found with an iterative modified Newton method. This approach only works for narrowband signals with small time delays. For larger time delays, strategies have to be employed to prevent phase aliasing.

However, if these approaches can be used, they are advantageous because they are very precise and have minimal computational complexity can be performed in a single step. In medical ultrasound, the backscattered signal is generally beam-formed along the axial direction, so these methods can only be used to calculate axial displacements. However, if unconventional beam forming strategies are used, phase can also be tracked in the lateral direction [8]. Alternatively, a synthetic oscillatory signal can be generated by taking the inverse Fourier transform of half the transformed signal [9]. Instead of the more prevalent cross-correlation/Fourier methods, Viola and Walker have worked on a sum-of-squared error/cubic spline method [10, 11]. After a cubic spline fit, the problem reduces to finding the roots of a polynomial whose order is proportional to the number of samples in the fit. In Viola and Walker's method, a continuous polynomial signal representation is compared to a discrete signal. Pinton and Trahey took a similar approach, but compared two continuous polynomial fits with the sum of squared differences and normalized cross-correlation [12].

#### **4.1.2 Parametric and non-parametric methods**

As studied in [10], a straightforward and computationally intensive approach to determine a precise signal shift is to resample the image through interpolation before performing cross-correlation. Use of a matched filter during resampling may improve the result [13]. Instead of resampling and recalculation of the cross-correlation, curve fitting can be applied. For example, a parabola [14, 15, 16, 17, 13] or cosine fit [18] can be used in 1D or an ellipsoid in 2D [19].

These methods are computationally efficient and easy to implement, but they suffer from bias errors because the underlying signal may not conform to the shape chosen [20, 21, 15, 17, 1].

Curve fitting bias errors can be avoided by using signal reconstruction with sinc interpolation, which is the maximum likelihood estimator for interpolation [1, 14]. Cespedes et al. examined the use of 1D sinc reconstruction to locate the cross-correlation peak, and found that it significantly out-performs parabolic or cosine interpolation. Reconstruction is computationally expensive, when compared to curve fitting methods, and an optimization method must be utilized to find the peak location. Cespedes et al. used a binary search method to decrease computation times [1].

It has also been demonstrated that a simultaneous two-dimensional (2D) displacement vector estimate will generate better results than two independent 1D displacement estimates [22, 9, 21, 20]. Sumi described an iterative 2D phase tracking technique [23], and Ebbini describes a similar technique that iteratively searches for the location where the gradient vectors of the 2D complex cross correlation are orthogonal, which exists along the zero-phase contour [24].

In this chapter, we propose the use of a 2D sinc reconstruction method coupled with traditional numerical optimization techniques for subsample ultrasound displacement estimation. Since parabolic methods remain the most popular method referenced in the literature and to follow the analysis of Cespedes et al. [1], we compare the new method with parabolic and cosine curve fitting. Performance is evaluated utilizing the variation in the elastographic signal-to-noise ratio ( $SNRe$ ) in tissue-mimicking (TM) experimental phantoms and numerical simulations. We examine the optimal sinc-filtering window radius and type, and the computational performance of the Nelder-Mead simplex and a regular step gradient descent optimizer.

## 4.2 2D sinc interpolation with numerical optimization

In the article by Cespedes et al. [1], a binary search algorithm improved the time required to localize the subsample 1D cross-correlation peak. We framed this process as a multi-parameter, single-valued cost function numerical optimization problem. We applied traditional numerical optimization methods that have quicker convergence properties than a binary search and can be applied to multiple parameters. The cost function to be maximized is the cross-correlation function. The parameters to be optimized are the axial and lateral displacements.

We obtained subsample displacements values with 2D sinc interpolation [25, 26]. The sinc kernel,  $K(t)$  is given by

$$K(t) = w(t)\text{sinc}(t) = w(t)\frac{\sin(\pi t)}{\pi t}$$

*Eqn. 4.1*

where  $w(t)$  denotes the window function. We examined different window functions shown in Table 4.1 [25, 26], Here  $m$  is the window radius; the window is non-zero from  $-m$  to  $m$ .

Window Name	Expression
Blackman	$0.42 + 0.50 \cos\left(\frac{\pi x}{m}\right) + 0.08 \cos\left(\frac{2\pi x}{m}\right)$
Cosine	$\cos\left(\frac{\pi x}{2m}\right)$
Hamming	$0.54 + 0.46 \cos\left(\frac{\pi x}{m}\right)$

Lanczos	$\text{sinc}\left(\frac{\pi x}{m}\right)$
Welch	$1 - \frac{x^2}{m^2}$

**Table 4.1:** Sinc window functions.

An interpolated normalized cross-correlation value,  $XCORR(x,y)$  was calculated with the sampled correlation values across the radius, and the window,

$$XCORR(x,y) = \sum_{i=\lfloor x \rfloor + 1 - m}^{\lfloor x \rfloor + m} \sum_{j=\lfloor y \rfloor + 1 - m}^{\lfloor y \rfloor + m} XCORR_{i,j} K(x-i)K(y-j)$$

*Eqn. 4.2*

In this chapter, two simple optimization methods were examined: a regular-step gradient descent and Nelder-Mead simplex (amoeba) optimization. In the regular-step gradient descent method, parameters are advanced along the direction of the negative of the gradient, which is calculated with the finite difference method. The step length is reduced by half when the sign of the gradient changes [27]. The well-known Nelder-Mead simplex optimization advances a three-point simplex over the optimization space.

We set the initial condition to be the sampled maximum of the normalized cross-correlation. The parameter space was the displacement in the axial and lateral directions defined in fractional samples. We proceeded with optimization until reaching convergence, which was defined with a minimum step length during the regular-step gradient descent method and a parameter tolerance with the Nelder-Mead simplex method.

### 4.3 Numerical properties of 2D sinc interpolation

### 4.3.1 Motion tracking algorithm used in testing

The proposed subsample interpolation algorithm was used within an ultrasound block-matching motion tracking context, the algorithm described in Chapter 9. Normalized cross-correlation was used as a similarity metric when comparing the matching blocks in the pre-deformation image to the image content in the post-deformation image search region. A multi-level tracking approach was used to improve search region initialization at the lowest level of the multi-level image pyramid. A three-level pyramid was utilized where the highest level was decimated by a factor of three in the axial direction and a factor of two in the lateral direction, and the middle level was decimated by a factor of 2 in the axial direction only. Before decimation, the data was filtered with a discrete Gaussian with variance  $(f/2)^2$ , where  $f$  is the decimation factor [28]. Matching-block sizes varied linearly from the top to bottom level with axial length of 1.3 mm and lateral width of 4.0 mm at the top level to an axial length of 0.5 mm and lateral width of 2.2 mm at the bottom level. There was no block overlap.

To remove peak-hopping tracking errors, displacements with strains greater than 15% magnitude were replaced with linearly interpolated values from outside the erroneous region. To improve correlation, matching-blocks at lower levels were compressed according to the strain estimated at the previous level [29]. The matching block was scaled by a factor of  $1 + \varepsilon_d$ , where  $\varepsilon_d$  is the strain in direction  $d$ , at its center and resampled using sinc interpolation with a Lanczos window and radius four.

In order to demonstrate that the proposed method is effective in finding the subsample peak in situations other than normalized cross-correlation with ultrasound radiofrequency (RF) data, we also examined interpolation after regularization with the Bayesian regularization method described in Chapter 3 [30]. As noted in the results, two iterations of the regularization method

were applied to the normalized cross-correlation. The strain regularization sigma (SRS) parameter used in the algorithm was 0.15 in the axial direction and 0.075 in the lateral direction.

Effectiveness of the algorithm was tested on both TM phantom and simulated numerical ultrasound images.

### **4.3.2 Tissue-mimicking phantom**

We collected ultrasound RF data on a TM phantom using a clinical ultrasound scanner, the Siemens S2000 (Siemens Ultrasound, Mountain View, CA, USA). The Siemens VFX9-4 linear array transducer acquired RF data at 40MHz with an excitation frequency of 8.9 MHz and at a depth of 5.5 cm.

A 95×95×95 mm, uniformly elastic oil-gelatin phantom was placed in a rigid, low-friction container and imaged from the top surface. Uni-axial, uniform, unconstrained compressions were applied by placing the surface of the transducer in an acrylic plate. Slip boundary conditions were maintained at the interface of the phantom and plate by ensuring adequate oil was present for lubrication. Precise deformations in the directions intended were achieved by a motion table with three linear degrees of freedom and two rotational degrees of freedom. A reference RF frame was collection along with post-deformation frames at 0.5%, 1.0%, 3.0%, 5.0%, and 7.0% axial strain magnitude. The position of the transducer was rotated and translated to obtain an uncorrelated scattering field, and the set of deformed frames re-collected. This process was repeated to obtain 30 independent trials at each applied deformation.

A TM phantom with a spherical inclusion, a common test object for ultrasound elastography, was also imaged. The inclusion was stiffer than the background and the phantom was subjected to a compression of 1.0% axial strain.



### 4.3.3 Ultrasound and mechanics simulation

Computer simulations were also performed intended to model the ultrasound and mechanical behavior of the clinical system and TM phantom. A numerical phantom was generated by simulating randomly positioned acoustic scatterers over a  $40 \times 40 \times 10$  mm volume. A transducer was modeled with a Gaussian spectrum having a center frequency of 8.0 MHz and a 40% fractional bandwidth, 128 element linear array with 0.15 mm lateral by 10 mm elevational element dimensions, and 0.2 mm element pitch [31]. Focusing was fixed at a 20 mm depth.

Displacements were applied to the scatterers assuming uni-axial compression of an incompressible material, i.e. local orthogonal strains were opposite in sign and half the magnitude along the axial directions. The same deformations applied to the TM phantom were simulated. Axial displacements started from zero at the transducer surface to a negative value at the bottom of the simulated phantom and lateral displacements transitioned from negative to positive values across the phantom with zero lateral displacement at the lateral midline. New sets of randomly distributed scatterers were used to create 30 independent scattering fields with the corresponding RF data.

### 4.3.4 Behavior of optimization methods

Following the analysis by Cespedes et al. [1], we evaluated the effectiveness of the subsample interpolation method using the  $SNRe$  feature.

$$SNRe = \frac{m_{\varepsilon}}{s_{\varepsilon}}$$

*Eqn. 4.3*

The *SNRe* estimate was evaluated over the applied deformations examined for both the TM phantom and numerical simulation, along the axial and lateral directions, and with and without regularization. The normal strain,  $\epsilon$ , in direction  $x$  is the derivative of the displacement along direction  $x$ , and if multiplied by 100 represents the percent elongation of a material [32]. Twice the standard error calculated for the 30 trials examined in each experiment was displayed in resulting plots. Unless otherwise noted, a radius of four RF data samples was used with the Welch window and Nelder-Mead optimization.

Variations in the *SNRe* are used to compare sinc interpolation with numerical optimization via Nelder-Mead simplex or regular step gradient descent with parabolic interpolation, cosine interpolation, and no interpolation.

The *SNRe* was also used to evaluate the parameters of the algorithm. With a window radius of four samples, we compare the Blackman, Cosine, Hamming, Lanczos, and Welch windows types. The effect of window radius was examined along with the convergence tolerance.

Given a convergence tolerance of  $1e-5$  samples, we inserted time probes in our code to measure the average time required for convergence in an image on an Intel Core i5 CPU clocked at 3.2 GHz. We also measured the effect of the initial simplex offset on the number of iterations required for convergence when using the Nelder-Mead optimization method.

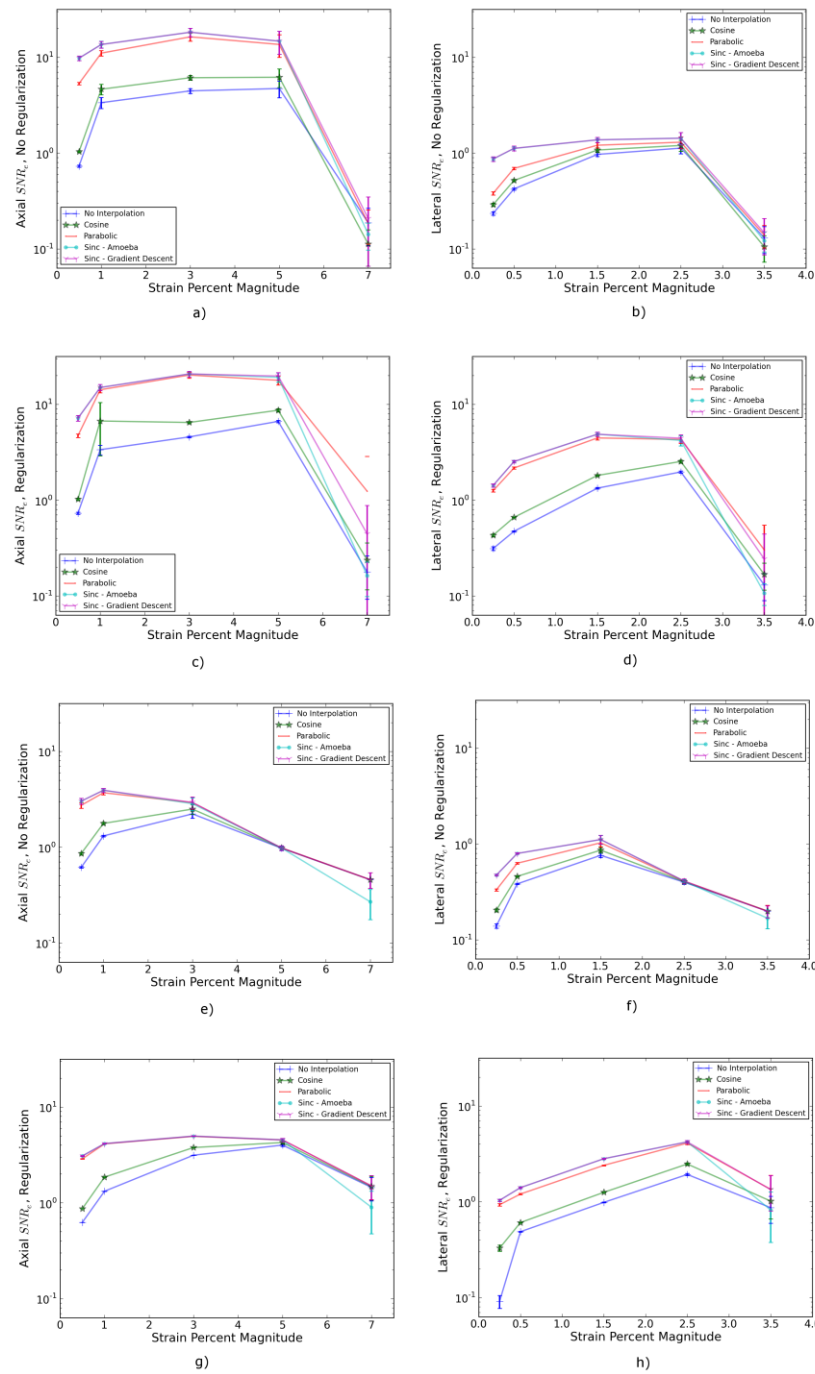


**Figure 4.1:** Performance of interpolation methods as compared using variations in the  $SNRe$  for 2D sinc interpolation using either Nelder-Mead simplex or regular-step gradient descent, parabolic interpolation, cosine interpolation, or no interpolation. a) TM phantom axial  $SNRe$  with no regularization, b) TM phantom lateral  $SNRe$  with no regularization, c) TM phantom axial  $SNRe$  with Bayesian regularization, d) TM phantom lateral

$SNRe$  with Bayesian regularization, e) simulation axial  $SNRe$  with no regularization, f) simulation lateral  $SNRe$  with no regularization, g) axial  $SNRe$  with Bayesian regularization, and h) lateral  $SNRe$  with Bayesian regularization.

The effectiveness of 2D windowed-sinc interpolation when compared to parabolic, cosine, or no interpolation is shown in Fig. 4.1. The  $SNRe$  is shown across the range of strains in both the lateral and axial directions. As shown in Fig. 4.1a), no interpolation provides the worst performance, followed by cosine interpolation, parabolic interpolation, and windowed-sinc interpolation. Lower  $SNRe$  arises for low strains from electronic and quantization noise artifacts and increased signal decorrelation due to larger applied deformation. For example, once we reach 7% applied deformation, motion tracking was no longer effective due to signal decorrelation [33]. For all the subplots shown in Fig. 4.1, sinc interpolation perform equally well regardless of the optimization method utilized. In the axial direction with no regularization, sinc interpolation is better than parabolic interpolation, but only significantly at lower applied deformation, e.g. 0.5% and 1.0%. Due to ultrasound's anisotropic resolution, lateral  $SNRe$  in Fig. 4.1b) is generally much lower than the axial  $SNRe$  as observed from Fig. 4.1a). However, the same trend in effectiveness observed in Fig. 4.1a) can be seen in Fig. 4.1b). In the lateral case, the benefits of sinc interpolation over parabolic interpolation are more dramatic. When regularization is applied in Fig. 4.1c) and d), the curves shift up as expected with improved  $SNRe$ . The same ranking that resulted in the no regularization case also occurs with regularization, although the difference between sinc and parabolic interpolation is reduced.

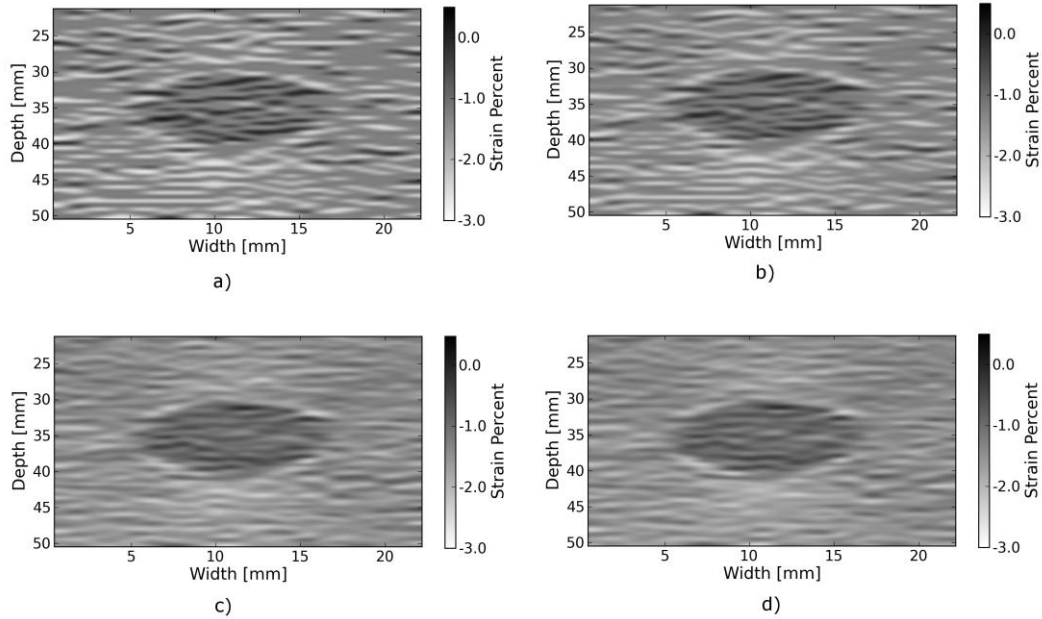


**Figure 4.2:** Axial strain distribution of an inclusion phantom subjected to 1.0% axial strain magnitude, with a) no interpolation, b) cosine interpolation, c), parabolic interpolation, and d) optimized sinc interpolation. Regularization was not applied in these images.

Images of the inclusion phantom's axial strain, Fig. 4.2, after compression to 1.0% strain reflect the outcomes on the uniform phantom. Image quality with no interpolation and cosine interpolation was significantly poorer than parabolic or sinc interpolation. The improvement of sinc interpolation over parabolic interpolation is less pronounced, but still significant. No regularization was applied, so some noise artifacts remain after sub-sample interpolation.

The dependence on the displacement convergence tolerance with the Nelder-Mead simplex optimization method was also studied. The tolerance is specified in units of data samples. Surprisingly, the  $SNRe$  is relatively stable across a range of values. Results in the regularization case and on simulation data were similar and are omitted for brevity. A tolerance of  $1e-5$  samples appears to be sufficient to generate consistent results.

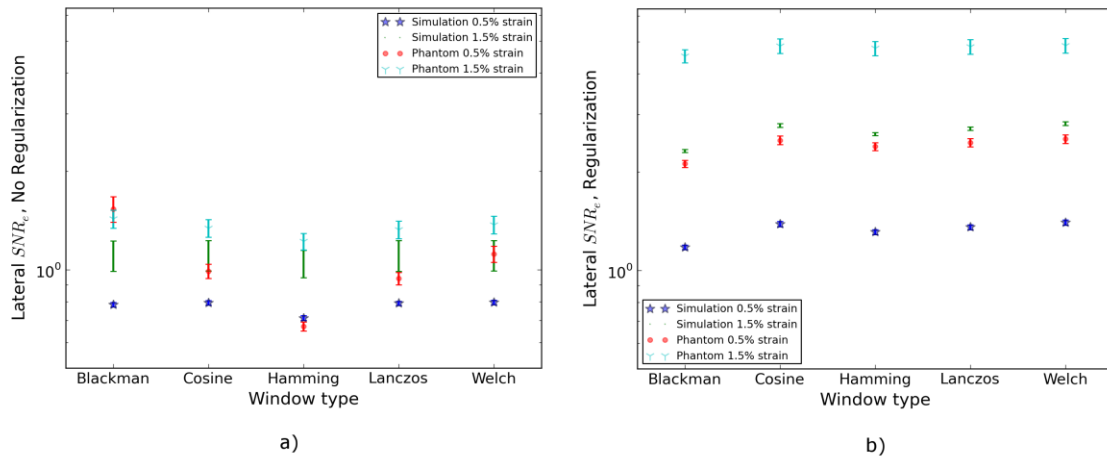


**Figure 4.3:** Impact of the sinc window type on lateral  $SNR_e$ . Statistically significant differences were not observed along the axial direction. a) lateral  $SNR_e$  with no regularization. b) lateral  $SNR_e$  with regularization.

The significance of the window type on the lateral  $SNR_e$  is displayed in Fig. 4.3. No significant impact was observed in the axial direction, and the lateral impact appears to be small but significant even though a generous radius of four samples was used. The Hamming window provides the worst performance, which is consistent with the study conducted by Meijering et al. where it was concluded that Welch, Cosine, and Lanczos windows are some of the best sinc approximation windows for medical images, while the Hamming is among the worst [25].

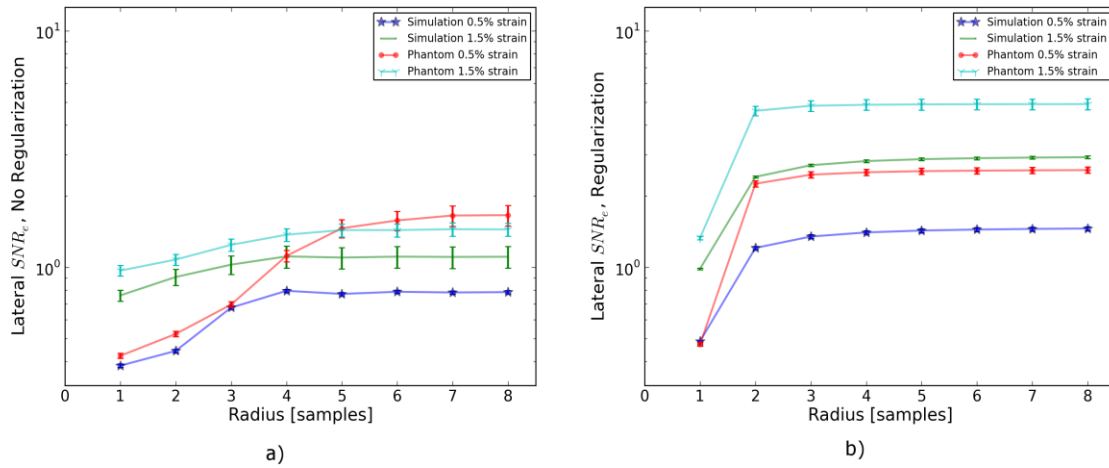


**Figure 4.4:** Impact of the sinc window radius in data samples. The radius is the same in all directions. a) lateral  $SNR_e$  with no regularization for the simulation and TM phantom with 0.5% and 1.5% nominal strain magnitude. b) the same quantity with regularization.

Content in the sinc interpolation calculation is determined by both the window type and the window radius. Figure 4 shows the effect of window radius in data samples on the lateral  $SNR_e$ . Axial  $SNR_e$  results are similar. For both the cases of regularization and no regularization, a radius of one or two samples is insufficient. In the case of no regularization, improvements appear up to a radius of five samples. In contrast, with regularization, little gain is accrued after three samples. This type of regularization localizes the content of the similarity function, which decreases the need for an expansive interpolation window.

Since the two optimization methods generate similar results, the preferred optimization method would be the one with improved computational efficiency. Table 3.0 shows mean optimization for a subsample displacement calculation. While sinc interpolation is much more computationally expensive than the parametric methods, the times required are still feasible for real-time imaging. Nelder-Mead simplex optimization is slightly faster than gradient descent

optimization, but they are very close. Figure 5 shows that the best initial simplex offset is approximately 0.2-0.3 samples. However, a poor choice for an initial simplex offset only generates about a 5% increase in optimization time.

Interpolation method	Mean optimization time [ $\mu$ s] $\pm$ 2*std. err.
Parabolic	$0.21 \pm 0.022$
Cosine	$1.07 \pm 0.021$
Sinc-Nelder-Mead	$261 \pm 5$
Sinc-gradient-descent	$277 \pm 6$

**Table 4.2:** Optimization times.

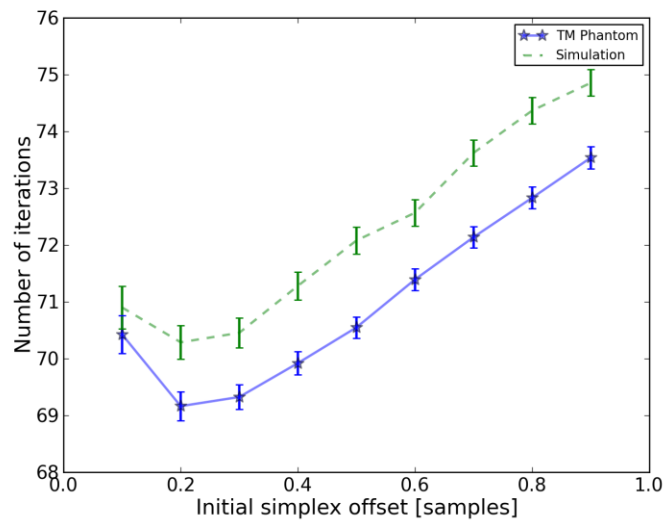


**Figure 4.5:** Number of iterations until convergence is reached given the initial simplex offset for both directions in samples.

## 4.4 Application of this method

Bias errors that occur with parametric interpolation methods can be attributed to a mismatch



between the underlying function being interpolated and the parametric model. While prior articles reported fewer bias errors with cosine interpolation relative to parabolic interpolation [1, 20], differences in the signal or sampling rate may explain the better performance attributed to parabolic interpolation. An advantage of sinc interpolation is that it is theoretically unbiased [1], and therefore will perform optimally despite the underlying signal. Unlike some of methods discussed in the Introduction, this method is not dependent on the similarity metric being normalized cross-correlation or the signal being narrowband. The approach was shown to be still applicable when regularization is applied. In addition, we perform 2D interpolation instead of separable 1D interpolations, which may help explain some improvement seen in the relatively noisy lateral direction.

Of course, real-world sinc interpolation has limitations due to quantization and finite window lengths. A similar approach that may have better performance is one that is incorporated into the motion-tracking algorithm by Brusseau et al. [34]. Determination of a subsample normalized cross-correlation peak is part of an optimization approach earlier in the process; with each subsample-shift calculation of the normalized cross-correlation involving resampling of the post-deformation image over the area of the matching-block. However, this has a significantly higher computational cost.

As shown in Fig. 4.1, as long the optimization method can robustly converge to the solution, the choice of optimization method does not affect the accuracy of the result. This particular problem is well-behaved and does not require complex optimization methods, with only two parameters, the axial and lateral displacements. If the problem is initialized close to the solution, and the similarity metric is smooth and without local maxima in the subsample location of the peak, the peak location is estimated accurately.

While 2D sinc-interpolation based subsample displacement estimation was not feasible in the past, acceleration of computation speeds and application of an optimization method make the method applicable to real-time imaging. Future advances in computing speed will occur with multi-core CPUs and general purpose GPUs (GPGPUs), so parallelization is an important property of an algorithm. The proposed algorithm is parallizable across each displacement pixel. In our tests, the Nelder-Mead simplex achieved convergence close to the gradient descent method. While gradient descent methods often converge with fewer iterations than gradient-free methods like the Nelder-Mead simplex, they also require calculation of the gradient at each iteration, which is computationally expensive in this case.

There is a tradeoff between accuracy and computational burden for the window length (radius) and convergence tolerance. A convergence tolerance of  $1e-5$  samples in each direction appears to be sufficient; no gains are observed with increasing tolerance. Diminishing returns will be obtained with a window radius higher than four samples. The Welch, Lanczos, or Cosine windows should be used to take the greatest advantage of the given radius, and the Hamming window should be avoided.

## 4.5 References

- [1] I. Cespedes, Y. Huang, J. Ophir and S. Spratt. Methods for estimation of subsample time delays of digitized echo signals. *Ultrasonic Imaging* 17, 142. 1995.
- [2] D. Maskell and G. Woods. The discrete-time quadrature subsample estimation of delay. *IEEE Transactions on Instrumentation and Measurement* 51, 133--137. 2002.
- [3] D. Maskell and G. Woods. The estimation of subsample time delay of arrival in the discrete-time measurement of phase delay. *IEEE Transactions on Instrumentation and Measurement* 48, 1227--1231. 1999.
- [4] S. Marple Jr. Estimating group delay and phase delay via discrete-time "analytic" cross-correlation. *IEEE Transactions on Signal Processing* 47, 2604--2607. 1999.
- [5] Pesavento. A time-efficient and accurate strain estimation concept for ultrasonic elastography using iterative phase zero estimation. *IEEE Transactions on Ultrasonics, Ferroelectrics, and Frequency Control* 46, 1057--67. 1999.
- [6] A. Grennberg, M. Sandell and S. Member. Estimation of Subsample Time Delay Differences in Narrowband Ultrasonic Echoes Using the Hilbert Transform Correlation. \*\* 41, 588--595. 1994.
- [7] J. Fromageau and P. Delachartre. Description of a new strain and displacement estimator for elastography. *2003 IEEE Symposium on Ultrasonics* 2, 1911--1914. 2003.
- [8] A. Basarab, P. Gueth, H. Liebgott and P. Delachartre. Phase-based block matching applied to motion estimation with unconventional beamforming strategies. *IEEE Transactions on Ultrasonics, Ferroelectrics, and Frequency Control* 56, 945--57. 2009.
- [9] X. Chen, M. J. Zohdy, S. Y. Emelianov and M. O'Donnell. Lateral speckle tracking using synthetic lateral phase. *Ultrasonics, Ferroelectrics and Frequency Control, IEEE Transactions on* 51, 540--550. 2004.
- [10] F. Viola and W. F. Walker. A spline-based algorithm for continuous time-delay estimation using sampled data. *IEEE Transactions on Ultrasonics, Ferroelectrics, and Frequency Control* 52, 80--93. 2005.
- [11] F. Viola, R. L. Coe, K. Owen, D. A. Guenther and W. F. Walker. Multi-Dimensional Spline-Based Estimator (MUSE) for Motion Estimation: Algorithm Development and Initial Results. *Annals of Biomedical Engineering* 36, 1942--1960. 2008.
- [12] G. F. Pinton and G. E. Trahey. Continuous delay estimation with polynomial splines. *IEEE Transactions on Ultrasonics, Ferroelectrics, and Frequency Control* 53, 2026--35. 2006.
- [13] X. Lai and H. Torp. Interpolation methods for time-delay estimation using cross-correlation method for blood velocity measurement. *IEEE Transactions on Ultrasonics, Ferroelectrics and Frequency Control* 46, 277--290. 1999.
- [14] R. Boucher and J. Hassab. Analysis of discrete implementation of generalized cross correlator. *Acoustics, Speech and Signal Processing, IEEE Transactions on* 29, 609--611. 1981.
- [15] G. Jacovitti. Discrete time techniques for time delay estimation. *IEEE Transactions on Signal Processing* 41, 525--533. 1993.

- [16] S. G. Foster, P. M. Embree and W. R. O'Brien. Flow velocity profile via time-domain correlation: error analysis and computer simulation. *IEEE Transactions on Ultrasonics, Ferroelectrics, and Frequency Control* 37, 164--75. 1990.
- [17] R. Moddemeijer. On the determination of the position of extrema of sampled correlators. *Signal Processing, IEEE Transactions on* 39, 216--219. 1991.
- [18] P. G. M. de Jong, T. Arts, A. P. G. Hoeks and R. S. Reneman. Determination of tissue motion velocity by correlation interpolation of pulsed ultrasonic echo signals. *Ultrasonic Imaging* 12, 84--98. 1990.
- [19] G. Giunta. Fine estimators of two-dimensional parameters and application to spatial shift estimation. *IEEE Transactions on Signal Processing* 73, 57--3207. 1999.
- [20] R. Zahiri-Azar, O. Goksel, T. S. Yao, E. Dehghan, J. Yan and S. E. Salcudean. Methods for the estimation of sub-sample motion of digitized ultrasound echo signals in two dimensions. *IEEE Engineering in Medicine and Biology Society. Conference* 2008, 5581--4. 2008.
- [21] B. J. Geiman, L. N. Bohs, M. E. Anderson, S. M. Breit and G. E. Trahey. A novel interpolation strategy for estimating subsample speckle motion.. *Physics in medicine and biology* 45, 1541--52. 2000.
- [22] E. Konofagou and J. Ophir. A new elastographic method for estimation and imaging of lateral displacements, lateral strains, corrected axial strains and Poisson's ratios in tissues. *Ultrasound in Medicine & Biology* 24, 1183--1199. 1998.
- [23] C. Sumi. Fine Elasticity Imaging Utilizing RF-echo Phase Matching Method. *IEEE Transactions on Ultrasonics, Ferroelectrics and Frequency Control* 46, 158--166. 1999.
- [24] E. Ebbini. Phase-coupled two-dimensional speckle tracking algorithm. *IEEE Transactions on Ultrasonics, Ferroelectrics and Frequency Control* 53, 972--990. 2006.
- [25] E. Meijering, W. Niessen, J. Pluim and M. Viergever. "Quantitative comparison of sinc-approximating kernels for medical image interpolation". In (Eds.) *Medical Image Computing and Computer-Assisted Intervention--MICCAI'99*, : Springer. 1999.
- [26] T. S. Yoo, M. J. Ackerman, W. E. Lorensen, W. Schroeder, V. Chalana, S. Aylward, D. Metaxes and R. Whitaker. "Engineering and Algorithm Design for an Image Processing API: A Technical Report on ITK - The Insight Toolkit". In Westwood, J. (Eds.) *Medicine Meets Virtual Reality*, Amsterdam: IOS Press. 2002.
- [27] L. Ibanez, W. Schroeder, L. Ng and J. Cates. The ITK Software Guide. 2005.
- [28] T. Lindeberg. *Scale-Space Theory in Computer Vision*. : Springer. 1994.
- [29] P. Chaturvedi, M. F. Insana and T. J. Hall. 2D companding for noise reduction in strain imaging. *IEEE Transactions on Ultrasonics, Ferroelectrics, and Frequency Control* 45, 179--191. 1998.
- [30] M. McCormick, N. Rubert and T. Varghese. Bayesian Regularization Applied to Ultrasound Strain Imaging.. *IEEE Transactions on Bio-medical Engineering* , . 2011.
- [31] Y. Li and J. A. Zagzebski. A frequency domain model for generating B-mode images with array transducers. *IEEE Transactions on Ultrasonics, Ferroelectrics, and Frequency*

*Control* 46, . 1999.

[32] W. M. Lai, D. Rubin and E. Krempl. *Introduction to Continuum Mechanics*. : Elsevier. 1993.

[33] T. Varghese and J. Ophir. A theoretical framework for performance characterization of elastography: the strain filter. *IEEE Transactions on Ultrasonics, Ferroelectrics, and Frequency Control* 44, 164--72. 1997.

[34] E. Brusseau, J. Kybic, J. Deprez and O. Basset. 2-D locally regularized tissue strain estimation from radio-frequency ultrasound images: theoretical developments and results on experimental data. *IEEE Transactions on Medical Imaging* 27, 145--60. 2008.